Check for updates

Optical dosimeter for selective retinal therapy based on multi-port fiber-optic interferometry

UIHAN KIM,[1,4] MINSUNG KWON,[1,4] GYEONGYEON JUNG,[2] YOUNGNAM KIM,[2] YUNAM LEE,[1] SEONGHUN IM,[1] BARRY CENSE,[1,3] 🆔 HYUNGSUK LEE,[1] WON-SUK OHM,[1] AND CHULMIN JOO[1,*]

[1]*Department of Mechanical Engineering, Yonsei University, 50 Yonsei-ro, Seodaemun-gu, Seoul, 03722, Republic of Korea*
[2]*Department of Research, Lutronic Corporation, 219 Sowon-ro, Goyang, 10534, Republic of Korea*
[3]*Optical and Biomedical Engineering Laboratory, Department of Electrical, Electronic & Computer Engineering, The University of Western Australia, Perth, WA 6009, Australia*
[4]*These authors contributed equally to this work*
[*]*cjoo@yonsei.ac.kr*

Abstract: Selective retinal therapy (SRT) employs a micro-second short-pulse lasers to induce localized destruction of the targeted retinal structures with a pulse duration and power aimed at minimal damage to other healthy retinal cells. SRT has demonstrated a great promise in the treatment of retinal diseases, but pulse energy thresholds for effective SRT procedures should be determined precisely and in real time, as the thresholds could vary with disease status and patients. In this study, we present the use of a multi-port fiber-based interferometer (MFI) for highly sensitive real-time SRT monitoring. We exploit distinct phase differences among the fiber ports in the MFI to quantitatively measure localized fluctuations of complex-valued information during the SRT procedure. We evaluate several metrics that can be computed from the full complex-valued information and demonstrate that the complex contour integration is highly sensitive and most correlative to pulse energies, acoustic outputs, and cell deaths. The validity of our method was demonstrated on excised porcine retinas, with a sensitivity and specificity of 0.92 and 0.88, respectively, as compared with the results from a cell viability assay.

1. Introduction

The retina is a multilayered structure of nerve tissue composed of a plexiform layer, photoreceptor layer (PRL), and retinal pigment epithelium (RPE). The RPE, located in the outermost part of the retina, is responsible for PRL homeostasis by phagocytizing worn-out photoreceptor disks and supplying nutrients or oxygen to the PRL [1,2]. With the progress of diabetes or aging, the number of dysfunctional RPE cells with metabolic fatty end-products increases [3,4]. Clinical studies have reported that this RPE malfunction plays a significant role in the development of common retinal disorders, such as diabetic macular edema (DME), age-related macular degeneration (AMD), and central serous retinopathy (CSR) [5–7].

Laser photocoagulation (LPC) has been regarded as the standard treatment method for these pathologies because of its intravitreal injection-free operation and selectivity [8,9]. LPC employs focused light with an exposure time of 50-200 milliseconds to induce photothermal necrosis of target tissue. It has proven its efficacy in the treatment of DME, CSR, and other retinal pathologies [10–13]. Among its various applications, LPC-based RPE regeneration has been extensively explored [14,15]. Similar to other epithelia, RPE cells can regenerate and proliferate, eventually being fully recovered [16,17]. Yet, considering that LPC can cause irreversible and permanent damage on healthy retinal cells and result in scotomata, reduced night vision, or unrecoverable central vision loss, therapeutic strategies capable of confining the photothermal

denaturation to RPE cells only would be highly desired for pathologies such as DME or CSR [18–20].

Selective retina therapy (SRT) with a pulse duration close to or shorter than the thermal relaxation time of RPE (μs-regime) has thus been suggested [21,22]. SRT targets melanosomes in RPE cells that absorb green light approximately seven times more than other retinal cells [23]. Focused illumination with a pulsed laser with a duration in the microsecond regime successfully restricts photothermal effect to RPE cells [22,24], and therefore can selectively necrotize targeted RPE cells, while reducing thermal dissipation and unintentional damage to the surrounding structures such as the PRL. The laser pulses with a pulse duration in the microsecond or sub-microsecond regime induce the formation of microbubbles in pigmented cells only, and the intracellular microbubbles then disrupt the cellular membrane by their growth and coalescence, leading to cell necrosis [25–28]. Various preclinical and clinical studies have demonstrated the potential of SRT for the treatment for DME and CSR [29–31].

In order to achieve reliable procedures and favorable prognosis of SRT, precise control of the SRT laser dose is essential [22,24,32]. The combination of ophthalmoscopy and fluorescein angiography (FA) has conventionally been employed to evaluate SRT outcomes, i.e, pulse-induced RPE damage [32–35]. The white burn mark of coagulated surrounding proteins has been used as an indicator of RPE damage, but may have been the result of an overdose of pulse energy, possibly impairing nearby cells. FA can validate membrane disruption, but it is only applicable at least 2 hours after SRT treatment [36]. Based on the high correlation between cell death and microbubble formation in RPE cells, several recent studies have demonstrated the use of photoacoustic (PA) detection for SRT dosimetry [24,37]. An ultrasonic transducer (UT) coupled with a contact lens was adopted to detect the PA pressure waves generated during SRT treatment. The method requires a physical contact to a cornea for sensitive PA detection, and demonstrated high sensitivity and correlation with RPE cell death.

Various optical techniques have been developed to realize non-contact SRT monitoring. Optical coherence tomography (OCT) has been employed to measure laser-induced modulation of tissue scattering properties after pulse irradiation [38–40]. Fluctuation in A-line intensity suggests microstructural change and vibration of tissue after the SRT pulse illumination. Optical reflectometric schemes have also been presented as non-contact optical detectors. They measure the intensity fluctuation of SRT pulsed laser due to the microbubble formations during SRT procedure [41,42]. Both OCT and optical reflectometry have demonstrated their prominent performance with high sensitivity to the laser-induced photothermal dynamics [40,42]. Furthermore, their feasibility in pre-clinical and clinical environments has been proved [31,40,42–44]. Conventional OCT systems, however, with an A-line rate of tens of kHz may not sufficiently resolve the laser-induced cavitation dynamics with a frequency range of several MHz [39,40,45]. In the case of optical reflectometry, the measurement time is set by the pulse duration of the SRT treatment laser itself, which is generally about several microseconds. Given that SRT pulse-induced cavitation and subsequent tissue modulations exhibit a lifetime longer than 10 μs [27,46], it would be beneficial to use a separate light source for SRT monitoring, thereby extending the measurement time.

In this study, we describe a novel SRT detection scheme based on a multi-port fiber-based interferometer (MFI) operating with a separate probe light source. The method uses distinct phase differences among the fiber ports in the MFI to quantitatively measure fluctuations of complex-valued information due to tissue deformation and cavitation dynamics. The MFI allows for the access of full complex-valued information, which enables evaluation of various metrics that are highly sensitive and correlative to SRT-induced cell deaths. Moreover, the extended measurement time, enabled by the use of a separate light source, allows for the detection of various dynamic signatures with longer time scales (and thus high frequency resolution) during and after the treatment pulse. We present the MFI-based experimental setup and analysis of

various metrics developed to correlate with SRT outcomes. The viability of our method was demonstrated through experiments utilizing excised porcine retinal tissues.

2. Setup and methods

2.1. Experimental setup

Figure 1(a) depicts a schematic of the MFI-based SRT monitoring setup. We employed a 3×3 fiber-optic coupler (SS85AV0303C3211, AC Photonics, USA) to build an MFI-based interferometer, but any multi-port fiber coupler can be used as long as the number of ports at one side exceeds two. A 825-nm single-mode fiber-coupled laser diode (LP830-SF30, Thorlabs, USA) was used as the probe and it was coupled to an optical circulator (VCIR-3-827-S-L-10-FA, Ascentta, USA). The probe light was then directed to the 3×3 fiber-optic coupler. The power stability of the laser source was measured to be <2%, and the coherence length of the probe light was measured to be 150 μm in air. We also quantified the fluctuation of the power spectrum of the probe laser, and determined that the fluctuation was smaller than 2% over its spectral bandwidth. The reference and sample arms were implemented in the output ports P_4 and P_5 of the coupler, respectively, and the P_6 port was not used (Fig. 1).
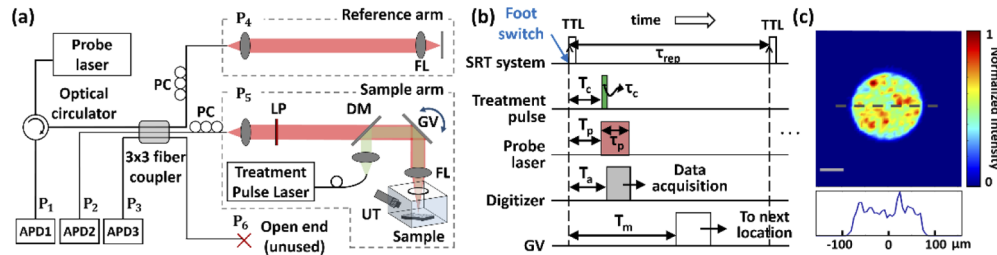

Fig. 1. (a) A schematic of MFI-based SRT monitoring setup based on a 3×3 fiber-optic coupler, APD1-3: avalanche photodiodes, PC: polarization controller, LP: long-pass filter, M: mirror, DM: dichroic mirror, GV: galvanometric beam scanner, FL: focusing lens, UT: ultrasound transducer. (b) Timing diagram for MFI signal acquisition. τ_{rep}: 10 ms, τ_c: 1.7 μs, τ_p: 30 μs, T_c: 800 μs, T_p: 790 μs, : 795 μs, T_m: 5 ms. (c) Spatial intensity map of the treatment laser beam measured in the sample plane. The beam diameter was measured to be 163 μm. The scale bar denotes 50 μm.

In the reference arm, we placed a mirror in the focal plane of a focusing lens (AC254-030-B-ML, Thorlabs, USA), and its position was finely tuned via a manual linear stage (M-423/M, Newport, USA) until the back-reflected light intensity measured at a detection port of the fiber coupler was maximized. In the sample arm, a 527 nm treatment beam from a frequency-doubled ND:YLF laser-based SRT system (Lutronic, Goyang, South Korea) was guided to the MFI system via an optical fiber with a core diameter of 50 μm. The beam was collimated with a collimator with a focal length of 10 mm, and was combined with the probe light through a dichroic mirror (AT565DC, Chroma, USA). The treatment laser was triggered by a manual footswitch and operated at a pulse duration of 1.7 μs ($\tau_c = 1.7$ μs), a repetition rate of 100 Hz ($\tau_{rep} = 10$ ms), and as a pulse train of 15 pulses. Each pulse train was operated in energy ramping mode. In the energy ramping mode, the maximum pulse energy could be set by a user and the pulse energy linearly increased from 50% of maximum energy in step of 3.57% of the maximum energy. The minimum and maximum pulse energies employed in this study were 15μJ and 160 μJ, respectively. The co-axially aligned probe and treatment light were then reflected by a galvanometric mirror scanner (GVS002, Thorlabs, USA) and focused onto a specimen via an achromatic focusing lens (AC254-030-B-ML, Thorlabs, USA). We employed the focusing lens with a focal length of 30 mm and a numerical aperture of 0.39, to match the imaging condition of the human eye. An

eye chamber was filled with a saline solution (0.9% NaCl, Cleancle, South Korea). The retina specimen was precisely positioned in the focal plane of the focusing lens via a motorized linear stage (PT1-Z8, Thorlabs, USA) until the path-length of the sample relative to the reference mirror was matched by monitoring the magnitude and contrast of the interference signal. The distal tip of the optical fiber from the SRT instrument was imaged onto the specimen plane. To measure the beam profile, we acquired the image of the beam with a monochromatic camera with a pixel size of 5.5 µm (Lt225M, 2048×1088 pixels, Lumenera, Canada). The beam profile featured a top-hat response with a smooth edge (Fig. 1(c)). We then obtained a binary map from the measured beam intensity image by applying a mask that thresholds and selects the pixels above the maximum noise level. The maximum noise level was estimated from the image acquired without the SRT beam irradiation. The average diameter of the beam profile was found to be 163 µm. The intensity variation of the SRT treatment beam may occur due to speckle formation. We measured the intensity of SRT beams at 15 different locations in the specimen plane and found the variation to be <7.6%. The spatial intensity variation in a single SRT beam due to speckle was also examined for 25 beam spots, yielding a 2.33 peak-to-mean ratio on average (Fig. 1(c)). We defined this quantity as the intensity modulation factor (IMF). The probe beam featured a Gaussian intensity distribution with a $1/e^2$ diameter of 83 µm in the sample plane. The axial Rayleigh range for the probe beam was estimated to be 6.6 mm. The optical power of the probe beam irradiated on the sample was set to 2.5 mW, which is below the ANSI standard safety limit of 17.1 mW for the human eye with a duration shorter than 30 µs [47]. Note that the use of shorter illumination time allows for light illumination with a higher power, which increases signal to noise ratio, while still being below the ANSI standard safety limit.

Three avalanche photodetectors (APD1-3, APD120A/M, Thorlabs, USA) were used to acquire the interference signals in the three detection arms. We inserted two long-pass filters (AT575lp, Chroma, USA) in the detection path to prevent any leakage of the treatment beam into the detector. No leakage of the treatment light was measured in the detection ports even with a mirror placed in the sample plane. We also installed an ultrasound transducer (UT, V384-SU, Olympus) with a central frequency of 3.5 MHz in the eye chamber to simultaneously measure PA waves during SRT procedures. In Fig. 1(b), a timing diagram for the SRT monitoring system is depicted. Upon foot-based initial activation, the SRT treatment laser system generated a transistor-transistor logic (TTL) pulse and emitted a light pulse with a time delay of 800 µs (T_c = 800 µs). We directed the TTL pulse to a function generator (33422A, Keysight Technologies, USA) to produce a pulse to synchronously trigger a laser driver controller (LDTC0520, Teamwavelength, USA) for the probe laser and data acquisition with delays of 790 µs (T_p = 790 µs) and 795 µs (T_a = 795 µs), respectively. The signal outputs from the APDs and UT were then collected by two digitizers (ATS9350, Alazar Technologies, Canada) at a sampling rate of 100 MHz. After data acquisition, a DAQ device (PCIe6353, National Instrument, USA) was triggered to control the galvanometric beam scanners to move the laser beams to different location between the light pulses (T_m = 5 ms). The data acquisition and operation of galvanometric beam scanner were controlled by custom-written scripts implemented in MATLAB (R2020a, Mathworks, USA).

2.2. *Optical quadrature detection based on a 3 × 3 fiber-optic interferometer*

Under ideal assumptions, such as equivalent energy transfer and no energy loss of a 3 × 3 fiber-optic coupler, it has been shown that there is an intrinsic phase difference (IPD) of $2\pi/3$ between any pair of interference signals from different ports [48]. The IPD in a MFI can be readily derived from the conservation of energy. Some studies exploited this IPD to achieve optical quadrature detection [49–51]. For example, Ref. [50] reported on *in vivo* PA imaging based on a MFI, assuming equal power splitting ratios and negligible change in sample reflectivity.

In our case, the pulse-induced changes in the scattering properties and wavefront modulation of the backscattered probe light would result in a radical fluctuation in the sample reflectivity.

Therefore, we took the sample reflectivity into account to achieve accurate detection of complex information of back scattered light from a sample. Because the MFI is a homodyne interferometer, the interference signal measured at detection port P_n (I_n) can be expressed as follows [48]:

$$I_n = I_0 \left[\alpha_{14}\alpha_{4n} + \alpha_{15}\alpha_{5n}R + 2\sqrt{\alpha_{14}\alpha_{4n}\alpha_{15}\alpha_{5n}} \; \sqrt{R}cos\varphi_n \right] \qquad (1)$$

with $\varphi_n = \phi_s + \phi_n$ (n=1,2,3). Here, φ_n represents the phase of the interferometric signal detected at P_n, which is the sum of the phase fluctuation due to the sample response to the pulse irradiation (ϕ_s), and the phase shift produced by port-to-port transition at P_n (ϕ_n). In Eq. (1), I_0 is the intensity of the probe laser, R is the sample reflectivity, and α_{mn} is the energy transfer efficiency from the fiber port m to port n. α_{mn} can be obtained experimentally by connecting a light source to port m and measuring the output intensity at port n. The systematic constants based on the measured splitting ratios are presented in Table 1. One can note that the differences between constants, $\alpha_{14}\alpha_{4n}$ and $\alpha_{15}\alpha_{5n}$ are smaller than $< 1.5\%$ for all the detection ports. Therefore, we assumed that $\alpha^2 \approx \alpha_{14}\alpha_{4n} \approx \alpha_{15}\alpha_{5n}$ (for $n = 1$, 2, and 3). Assuming the equal energy transfer efficiency between the ports, the IPD between port P_n and P_m ($\Delta\phi_{nm} = \phi_n - \phi_m$) can be approximated to be $2\pi/3$, and then, one can obtain:

Table 1. Experimentally measured constants for our MFI setup

Detector	$\alpha_{14}\alpha_{4n}$	$\alpha_{15}\alpha_{5n}$	$\sqrt{\alpha_{14}\alpha_{4n}\alpha_{15}\alpha_{5n}}$
1	0.1197	0.1176	0.2373
2	0.1148	0.1140	0.2227
3	0.1090	0.1155	0.2244

$$2I_1 - I_2 - I_3 = 6\alpha^2 \, Re\,(Z)$$
$$I_3 - I_2 = 2\sqrt{3}\alpha^2 \, Im(Z) \qquad (2)$$

where the complex-valued information Z is given as:

$$Z = \left[I_0\sqrt{R} \right] e^{j\phi_s}. \qquad (3)$$

The phase of Z (ϕ_s) can then be obtained as:

$$\phi_s = tan^{-1} \left[\frac{\sqrt{3}\,(I_3 - I_2)}{2I_1 - I_2 - I_3} \right]. \qquad (4)$$

Note that the derivation of Eq. (2–4) is similar to that described in Ref. [50].

To validate quadrature detection capability of our MFI, we performed the experiment as done in Ref. [48] to measure the IPDs. A mirror was placed in the sample arm, and the interference signals were measured while scanning the reference mirror at a constant velocity of 2.6 mm/s with a motorized linear actuator (Z825B, Thorlabs, USA). We measured sinusoidal intensity oscillations at all the detection ports and quantified the phase differences among the signals, yielding $\Delta\phi_{12} = 120°$ and $\Delta\phi_{23} = 118°$ (Fig. 2(a)). Based on the Eq. (2)-(4), the amplitude and the phase of the complex information Z were also retrieved (Fig. 2(b)). While the amplitude was constant with less than 2.9% variation during the mirror scan, the unwrapped phase exhibited a linear behavior as the reference mirror moved at the constant velocity. The experimentally acquired Doppler shift was 6.10 kHz, which was close to the estimated value of 6.12 kHz.
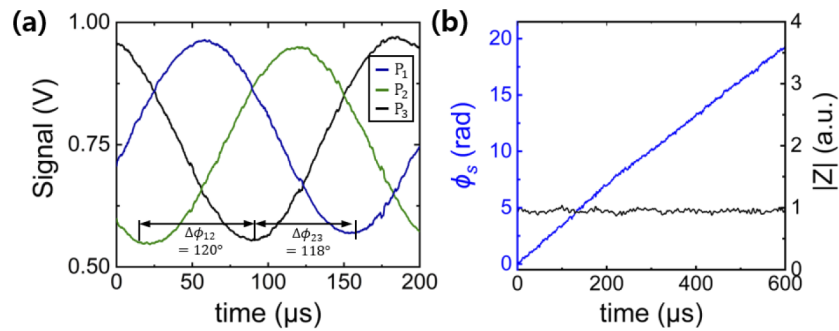
Fig. 2. (a) Measured interferometric signals at the three detection ports, while scanning the reference mirror at a constant velocity of 2.6 mm/s. (b) Retrieved magnitude($|Z|$) and phase (ϕ_s).

2.3. Sample preparation and LIVE/DEAD assay

Pig eyes were collected from a local slaughterhouse within 6 hours after enucleation. The anterior segment of the globe and the vitreous body were removed, and the upper retinal layers containing fibrosis and neural retinal layer were carefully peeled off for direct access to RPE cells. The RPE-choroid-sclera segments were then positioned in an eye chamber filled with saline solution. They were then irradiated by the SRT treatment light with various pulse energies with values ranging from 15 to 100 µJ in the ramping mode.

After SRT treatment, cell viability was tested using the LIVE/DEAD Viability/Cytotoxicity Kit L3224 (Invitrogen, Paisley, UK). 2 µM of Calcein-AM and 4 µM of ethidium homodimer (EthD-1) were added to the RPE tissue samples and incubated for 20 minutes at room temperature. A fluorescence microscope (ECIPSE Ni-U, Nikon, Tokyo, Japan) equipped with a charge-coupled device camera (DS-Q1Mc, Nikon) was used to visualize live and dead cells stained in green and red, respectively.

Fluorescence images with RPE-unique honeycomb structures were selected for assessment of cell viability. According to the LIVE/DEAD assessment, the dataset consisted of 195 lesions from 13 different porcine eyeballs, including 121 positive and 74 negative.

3. Result

3.1. Quadrature detection of SRT response

Figure 3(a) shows a representative fluorescence image of retinal tissue after the SRT procedure in ramping mode (the pulse energy ranged from 50 µJ to 100 µJ). The damaged cells are visible in red. It can be seen from Fig. 3(a) that the damage radius increases with the applied pulse energy. This may be accounted for by a smooth edge profile of the SRT treatment beam. The complex-valued information from Eq. (3) was presented in a complex-time space for 20 µs (Fig. 3(b)). One can see that the Z was stable when there had been no SRT pulse irradiation, but fluctuated strongly after the pulse irradiation. This response may arise from photo-elastic shock waves and creation and collapse of microbubble clouds. The responses from the higher energy pulses exhibited more dramatic modulation in both amplitude and phase, which can be inferred from the large variations in rotational angle and length of the measured complex vector, respectively.

3.2. Evaluation of various metrics for SRT monitoring

Based on the measured complex information (Z), we evaluated several metrics to find the most sensitive and correlative one with applied pulse energies, UT outputs, and RPE cell deaths.
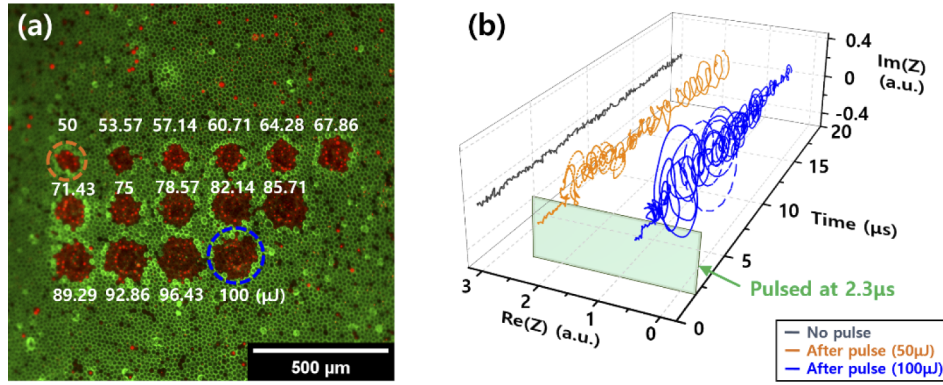
Fig. 3. (a) A representative fluorescence image of a retinal tissue after irradiation with an SRT pulse train in ramp mode (50-100 µJ). The applied pulse energy is presented proximal to each irradiated spot. The dead cells due to the application of the SRT laser pulse are visualized in red. (b) 3D perspective of the measured interference signals with no pulse irradiation (black), and after pulse irradiations with energies of 50 µJ (orange dot) and 100 µJ (blue dashed line). For clear visual comparison, the data with non-pulse and 50 µJ pulse irradiation were shifted by 1.5 and 3 in the real axis, respectively.

The first two metrics considered the magnitude ($|Z|$) and real part ($\text{Re}(Z)$) of the complex signal Z, which are utilized in conventional SRT monitors based on reflectometry [41,42] and low-coherence interferometry [27]. The two signals, $|Z|$ and $\text{Re}(Z)$, were acquired for 30 µs at different locations on the retina. The signals were then Fourier-transformed and their magnitudes were summed in the frequency range of 0.1–20 MHz. This frequency range for integration was determined based on previous reports that the SRT-induced acoustic waves have a frequency range of 0.1–20 MHz [27,33,46]. The mathematical definitions for the two metrics can be written as follows:

$$\hat{S}(|Z|) = \int_{f_{\min}}^{f_{\max}} |\tilde{F}(|Z|)| df$$

$$\hat{S}(\text{Re}(Z)) = \int_{f_{\min}}^{f_{\max}} |\tilde{F}(\text{Re}(Z))| df \tag{5}$$

where $\tilde{F}$ represents the Fourier transform operator and f_{min} and f_{max} define the frequency range for integration ($f_{min} = 0.1$ MHz and $f_{max}=20$ MHz in our case). The last metric evaluated was the complex contour integration (*CCI*) in the complex plane. As can be seen in Fig. 3, the complex vector Z undergoes rapid spiral motion in time, and its motion is more pronounced at higher pulse energies. Therefore, we considered the total trajectory length as a quantitative measure for the SRT results. In general, the phase offers higher sensitivity to a small perturbation of scattering surface than the amplitude, but it is more susceptible to noise, especially for signals with low SNRs. *CCI* is an effective and robust measure in the sense that it takes the modulation in the phase and magnitude of the complex signals into account, while minimizing the effect of the noise from the low-SNR signals. That is, the contour length of the complex signals with low SNR will be smaller and contribute less to the total contour length than that of the high-SNR signals. *CCI* is defined as

$$CCI = \sum_{n=0}^{N-1} |Z[(n+1)\Delta t] - Z[(n)\Delta t]| \tag{6}$$

where Δt is the time interval between two adjacent data points, and N is the total number of sampling points within measurement time (30 µs in our case) for a given Z.

3.3. SRT monitoring metrics versus SRT pulse energies and UT outputs

Having defined the metrics, we examined the dependence of each metric on the applied SRT pulse energies. A total of 195 interference signals were acquired at different locations on 13 porcine retinal specimens. We controlled a galvanometric beam scanner to move and illuminate a focused treatment laser pulse with different pulse energy in the range of 15 to 160 μJ. Figure 4 presents the metrics as a function of the applied pulse energy. Noise-equivalent SRT metrics were evaluated by computing the SRT metrics for the complex-valued information measured for 30 μs without SRT irradiation. The results were 209.33 for $\hat{S}(|Z|)$, 126.49 for $\hat{S}(\mathrm{Re}(Z))$, and 35.55 for *CCI*. The noise levels are presented in grey areas in Fig. 4. The black dotted lines are linear regression fits to the measured results. The correlation coefficients were found to be 0.54 for $\hat{S}(|Z|)$, 0.60 for $\hat{S}(\mathrm{Re}(Z))$, and 0.87 for *CCI*, suggesting that *CCI* is the most sensitive and correlative one with pulse energies among the metrics considered.
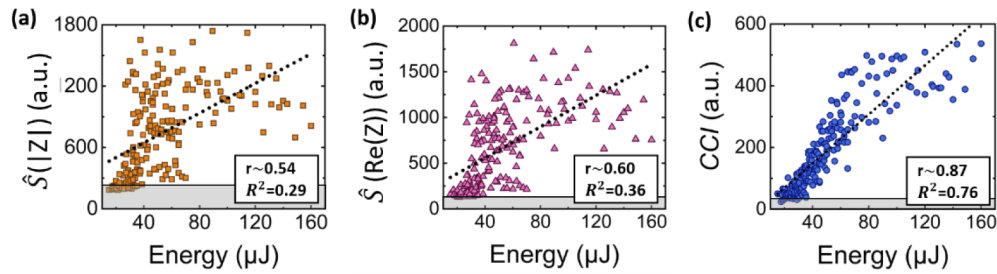

Fig. 4. Pearson correlation analysis with irradiated pulse energies and the SRT metrics. Black dotted lines represent linear fits. Pearson correlation coefficients (r) and R-square values are presented in insets. The shaded area in grey denote noise-equivalent SRT metrics.

One can see that *CCI* varied linearly at low pulse energies with a high sensitivity, but plateaued at higher pulse energies. We experimentally observed that the Z underwent a rapid spiral modulation in the complex plane as the pulse energy increased. However, with the pulse energies above 80 μJ, Z often rotated more than 2π (i.e., its phase is wrapped) at a certain instant, and the resultant *CCI*, which is the sum of the magnitudes of vector difference between two consecutive Zs, could not capture such large variations. In addition, the formation of microbubbles could hinder the back-scattered light to be measured, and the magnitudes of the complex vectors could thus be attenuated [45,52,53].

An UT has been extensively utilized in various clinical studies for SRT monitoring because of its high sensitivity and precision for RPE cell necrosis [24,31,37]. In order to validate our MFI-based metrics for SRT monitoring, we compared the results of our analysis against UT outputs. The UT signals (V_{UT}) acquired for 30 μs after a pulse irradiation were applied to the same signal analysis as with $|Z|$ and $\mathrm{Re}(Z)$; the measured UT signals were Fourier transformed, and its magnitudes were summed in the frequency range of 0.1–20 MHz to obtain UT output ($\hat{S}(V_{UT})$):

$$\widehat{S}(V_{UT}) = \int_{f_{\min}}^{f_{\max}} |\widetilde{F}(V_{UT})| \, df \qquad (7)$$

It can be noted that the measured UT output corresponded well to the applied pulse energies (Fig. 5). The UT output exhibited a low sensitivity in the low pulse energies but its sensitivity increased for the pulse energies above ~40 μJ. This indeed agrees to the observations in previous publications [54,55], and is different from those of our metrics in that our metrics exhibit high sensitivities in the low pulse energies, and the sensitivities become smaller in the high pulse energies (see Fig. 4). We further examined the correspondences of our metrics to the UT output

($\hat{S}(V_{UT})$) (Fig. 6). One can note that *CCI* exhibited the highest correlation with the $\hat{S}(V_{UT})$ (r = 0.88) among all the three metrics.
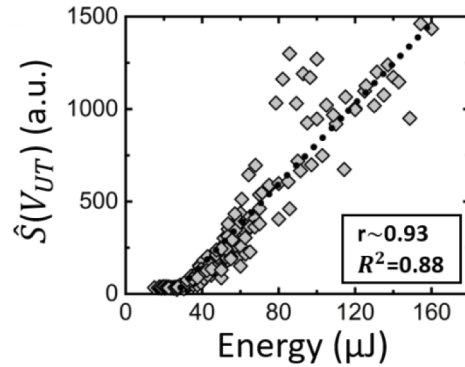

Fig. 5. $\hat{S}(V_{UT})$ as a function of the irradiated SRT pulse energy Pearson correlation coefficient (r) and R-square value are presented.
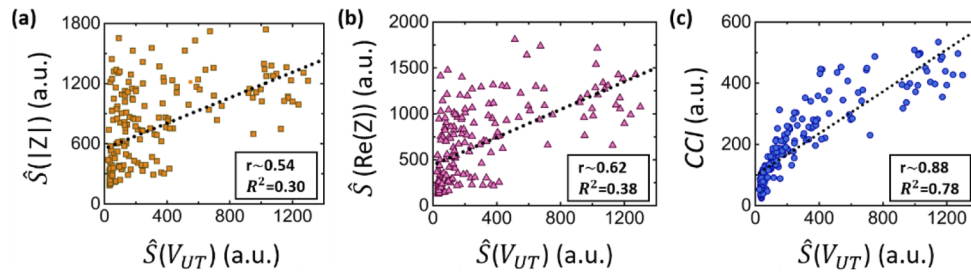

Fig. 6. Pearson correlation analysis with $\hat{S}(V_{UT})$ and the SRT metrics. Black dotted lines represent linear fits.

3.4. *SRT metrics versus RPE cell deaths*

A high correlation of a SRT metric with the applied pulse energies and $\hat{S}(V_{UT})$ may suggest its potential as a reliable SRT monitor. However, the higher correlation does not necessarily guarantee its high sensitivity and specificity for SRT-induced RPE cell damage. In order to assess the sensitivity and specificity, we performed receiver operating characteristic (ROC) curve analyses for the considered SRT metrics (Fig. 7). A total of 195 SRT-treated retinal lesions were examined through the LIVE/DEAD assay. In Fig. 7, among the considered SRT metrics, *CCI* exhibits a detection performance similar to $\hat{S}(V_{UT})$ with the highest area under the curve (AUC) value of 0.96. To compare the performances of each SRT metric, cut-off point (CP) for each SRT metric was set (Fig. 8). The CP was set to be the maximum Youden Index (J-index) that equally weights both selectivity and sensitivity [56]. Evaluated classification performances of each metric are shown in Table 2. *CCI* classified cell necrosis with an accuracy of 0.90, whereas the accuracies for $\hat{S}(|Z|)$, $\hat{S}(\text{Re}(Z))$, and $\hat{S}(V_{UT})$ were found to be 0.86, 0.86, and 0.90, respectively. In Table 2, other statistical values are presented in detail.

For automatic SRT dose control with energy ramping mode, clinicians may pre-set a threshold for a SRT metric to automatically stop the pulse train, when the output from the SRT metric exceeds the threshold [42,44]. For example, Seifert et al. [42] proposed an automated feedback control of SRT by measuring the backscattered light of the therapeutic pulsed laser, and using
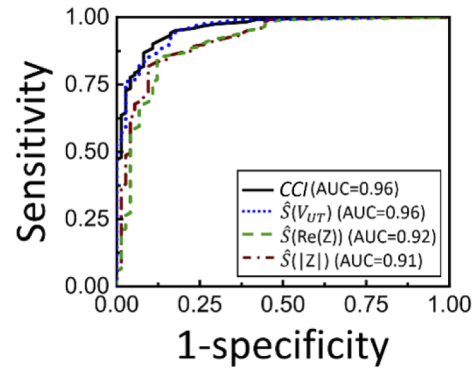
Fig. 7. Receiver operating characteristic (ROC) curve analysis for SRT metrics. The live and dead cells were enumerated from the fluorescence images of the retina tissues after SRT pulse irradiation.
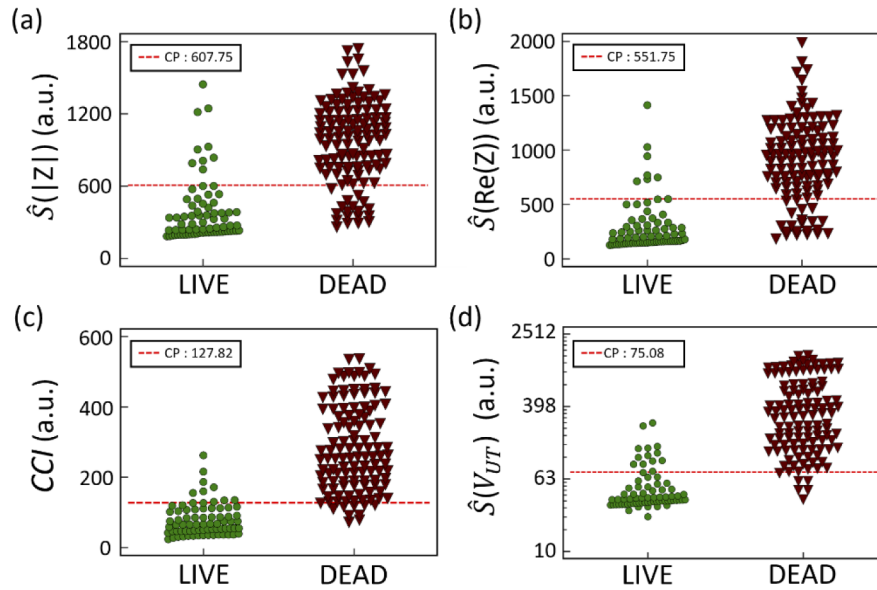

Fig. 8. (a)–(d) Classification results for 195 SRT retina lesions using the SRT metrics. The live and dead cells were enumerated with the fluorescence images after LIVE/DEAD assay. The dashed red lines denote the cut-off point (CP) acquired from the ROC curve analysis for each metric.

Table 2. Performance comparison of SRT metrics based on the set cut-off point.

	Accuracy	Sensitivity(=recall)	Specificity	Precision	F1-score
$\hat{S}(|Z|)$	0.86	0.85	0.88	0.92	0.88
$\hat{S}(\text{Re}(Z))$	0.86	0.83	0.90	0.93	0.88
CCI	0.90	0.92	0.88	0.93	0.92
$\hat{S}(V_{UT})$	0.90	0.95	0.82	0.90	0.92

the threshold twice as large as the CP optimized for J-index, false positives could be eliminated, while sensitivity was obtained as 0.88. In our case, we found that using the threshold of 1.25

times higher than the cut-off point optimized for J-index, only five false positives were found while the sensitivity stayed in a reasonable range (0.82). Further pre-clinical and clinical studies with MFI will be able to suggest an optimal threshold for automatic SRT dose control.

4. Discussion and conclusion

We presented a novel application of MFI for highly sensitive and precise SRT monitoring. Based on the distinct phase differences among the MFI fiber ports, the full complex-valued interferometric signal can be quantitatively measured. We acquired time-lapse fluctuations of the complex-valued information during SRT pulse irradiation and computed various SRT metrics to obtain one of the highest correlations with pulse energies, $\hat{S}(V_{UT})$, and RPE cell death. Among the metrics evaluated, we found that CCI exhibited the highest correlation with pulse energies, $\hat{S}(V_{UT})$, and RPE cell death.

Several optical dosimeters have been suggested previously. Neumann et al. [27], for instance, described a SRT dosimeter based on a Michelson interferometer. The method employed a separate light source for dosimetry, and measured the fluctuation of the real part of the interference signal upon SRT irradiation. The method computed a signal energy in a certain time window, and demonstrated its classification performance with less than 10% false negative or positive detection on excised porcine retina samples. In our case, we exploited a MFI to obtain both intensity and phase information based on the intrinsic phase difference in the MFI fiber ports. The full complex-valued information was then utilized to compute CCI, which is found to be more sensitive than other metrics based on the back-scattered intensity and real part of the interferometric signal.

Seifert et al. [42] also presented a simple reflectometric detection and algorithm for real-time SRT monitoring. It utilized the SRT treatment laser itself as the probe light source to determine if microbubbles were formed during irradiation, and demonstrated a sensitivity and specificity of 1 and 0.93, as compared with FA analysis. Our MFI-based detector uses a separate light source, and thus allows for the detection of various dynamics with longer timescales, which includes both cavitation dynamics and tissue deformation during and after the treatment pulse. Note that the pulse duration of SRT treatment laser is only 1.7 μs, whereas in our case the measurement time was 30 μs.

OCT-based dosimeters have been demonstrated as a viable SRT dosimeter. For a given M-mode OCT dataset, various signal processing schemes based on reflectivity and speckle variance have been developed to evaluate the SRT results [38,40,57]. Previous studies revealed that OCT measures thermal tissue vibration after SRT laser pulse irradiation, which may result from micro-cavitation as well, though its life time is much shorter than the OCT acquisition time [24,25,39,40]. Our method, on the other hand, exhibits a large detection bandwidth (3 dB bandwidth = 50 MHz), and therefore can directly measure fluctuations associated with cavitation dynamics, which exhibit a frequency range of several MHz. Recent developments in high-speed OCT systems based on, for example, Fourier domain mode-locked lasers with a sweep rate of ~100 MHz, may allow for OCT-based SRT monitoring with a larger detection bandwidth [58]. However, its implementation is costly and complicated.

We analyzed the dichotomous experimental data, i.e., 0 for living tissue and 1 for the dead lesion, obtained from the LIVE/DEAD assay for each applied pulse energy. A standard probit analysis [59] was carried out with a statistics program (SPSS statistics 26, IBM, USA), and the energy threshold for ED_{50} was 38.3 μJ, which corresponds to a mean radiant exposure of 183 mJ/cm^2 within measured beam area. The peak radiant exposure was 427.7 mJ/cm^2, taking the IMF (i.e., 2.33) into account [60]. For accurate SRT dose monitor, it is important to set the optimal beam spot sizes for the probe beam. If the number of RPE cells in the probe area is much smaller than the number of cells in the treatment beam spot, the measurement would not accurately reflect the SRT treatment process, which results in false negatives. Moreover, because

of the small number of RPE cells contributing to the signal, the sensitivity would also decrease. The use of the treatment and probe beams with the similar beam profiles and sizes would thus be desired.

To facilitate translation of our method into clinics, further improvements should be made in terms of its implementation and operation. We employed an interferometric setup with separate reference and sample arms which may be vulnerable to external noises such as temperature, vibration, and other sources of mechanical noise. In our setup, SRT treatment and probe beams were co-axially aligned and focused on the same location on the RPE layer. Moreover, the SRT pulse duration is shorter than the thermal diffusion time of RPE layer (~100 μs) [61]. Therefore, it is anticipated that temporal fluctuations of the complex-valued information would result largely from RPE cells being irradiated by the SRT laser. Nonetheless, MFI dosimetry with a light source with a short coherence length would further improve depth selectivity. In doing so, the interferometric signal is coherence-gated, thereby mitigating the noise from other retinal layers. On the other hand, MFI is very sensitive to relative displacement and tilt between the MFI-based optical setup and subject eye. Eye tracking systems can be utilized to initially position SRT treatment and probe beams on the targeted RPE cells, and our MFI dosimeter then measures rapid signal fluctuation during SRT procedures. Given the frequency range of bulk motions, drifts and tremor (< 200 Hz) [40,62–64], it is expected that such noise would not influence the high-frequency dosimetric signal being measured in the frequency range of 0.1–20 MHz.

It should be noted that the SRT instrument used in this study to deliver laser light to the sample is not the subject of our study, and rather our aim is to introduce a MFI for highly precise SRT dosimetry. MFI features high correlation with RPE cell deaths, a large detection bandwidth and a simple fiber-based implementation. Based on these features, we believe that MFI has the potential to be utilized for automated SRT dose control. MFI output can be acquired and processed in real time, and as soon as a *CCI* reaches a certain threshold, the treatment laser can be programmed to stop automatically. The threshold can also be pre-set or adjusted by the clinician to avoid undesired photocoagulation and damage to healthy tissue. Based on the demonstrated performance, our method may be used as a complementary means to existing SRT dosimeters. For instance, the method may be used jointly with a PA detector, thus cross-validating the formation of micro-bubbles and RPE cell deaths. Its application in preclinical studies is underway.

Disclosures. The authors declare that there are no conflicts of interest related to this article.

Data availability. Data underlying the results presented in this paper are not publicly available at this time but may be obtained from the authors upon reasonable request.

References

1. O. Strauss, "The retinal pigment epithelium in visual function," Physiol. Rev. **85**(3), 845–881 (2005).
2. R. H. Steinberg, "Interactions between the retinal pigment epithelium and the neural retina," Doc. Ophthalmol. **60**(4), 327–346 (1985).
3. G. Lutty, J. Grunwald, A. B. Majji, M. Uyama, and S. Yoneya, "Changes in choriocapillaris and retinal pigment epithelium in age-related macular degeneration," Mol. Vis. 5(35) (1999).
4. H. Z. Xu, Z. Song, S. Fu, M. Zhu, and Y. Z. Le, "RPE barrier breakdown in diabetic retinopathy: seeing is believing," J. Ocul. Biol. Dis. Infor. **4**(1-2), 83–92 (2011).
5. H. Funatsu, H. Yamashita, S. Nakamura, T. Mimura, S. Eguchi, H. Noma, and S. Hori, "Vitreous levels of pigment epithelium–derived factor and vascular endothelial growth factor are related to diabetic macular edema," Ophthalmology **113**(2), 294–301 (2006).
6. N. Golestaneh, Y. Chu, Y. Y. Xiao, G. L. Stoleru, and A. C. Theos, "Dysfunctional autophagy in RPE, a contributing factor in age-related macular degeneration," Cell Death Dis. **8**(1), e2537 (2018).

7. J. Lin and R. W. Chen, "Central Serous Chorioretinopathy," in *Manual of Retinal Diseases*, C. A. Medina, J. H. Townsend, and A. D. Singh, eds. (Springer, 2016), pp. 421–426.

8. P. Tababat-Khani, L. M. Berglund, C. D. Agardh, M. F. Gomez, and E. Agardh, "Photocoagulation of human retinal pigment epithelial cells in vitro: evaluation of necrosis, apoptosis, cell migration, cell proliferation and expression of tissue repairing and cytoprotective genes," PLoS One **8**(8), e70465 (2013).

9. Y. M. Paulus, A. Jain, R. F. Gariano, B. V. Stanzel, M. Marmor, M. S. Blumenkranz, and D. Palanker, "Healing of retinal photocoagulation lesions," Invest. Ophthalmol. Vis. Sci. **49**(12), 5540–5545 (2008).

10. E. T. D. R. S. R. Group, "Photocoagulation for diabetic macular edema," Arch. Ophthalmol. **103**(12), 1796–1806 (1985).

11. B. Nicholson, J. Noble, F. Forooghian, and C. Meyerle, "Central serous chorioretinopathy: update on pathophysiology and treatment," Surv. Ophthalmol. **58**(2), 103–126 (2013).

12. E. T. D. R. S. R. Group, "Early photocoagulation for diabetic retinopathy: ETDRS report number 9," Ophthalmology **98**(5), 766–785 (1991).

13. P. Sternberg Jr, D. P. Han, J. H. Yeo, C. C. Barr, H. Lewis, G. A. Williams, and W. F. Mieler, "Photocoagulation to prevent retinal detachment in acute retinal necrosis," Ophthalmology **95**(10), 1389–1393 (1988).

14. G. H. Bresnick, "Diabetic maculopathy: a critical review highlighting diffuse macular edema," Ophthalmology **90**(11), 1301–1317 (1983).

15. M. S. Figueroa, A. Regueras, J. Bertrand, M. J. Aparicio, and M. G. Manrique, "Laser photocoagulation for macular soft drusen. Updated results," Retina **17**(5), 378–384 (1997).

16. I. Grierson, P. Hiscott, P. Hogg, H. Robey, A. Mazure, and G. Larkin, "Development, repair and regeneration of the retinal pigment epithelium," Eye **8**(2), 255–262 (1994).

17. O. G. Stroeva and V. I. Mitashov, "Retinal pigment epithelium: proliferation and differentiation during development and regeneration," Int. Rev. Cytol. **83**, 221–293 (1983).

18. J. Marshall, "Thermal and mechanical mechanisms in laser damage to the retina," Invest. Ophthalmol. Vis. Sci. **9**(2), 97–115 (1970).

19. H. D. Kim, S. Y. Jang, S. H. Lee, Y. S. Kim, Y. H. Ohn, R. Brinkmann, and T. K. Park, "Retinal pigment epithelium responses to selective retina therapy in mouse eyes," Invest. Ophthalmol. Vis. Sci. **57**(7), 3486–3495 (2016).

20. I. Kozak and J. K. Luttrull, "Modern retinal laser therapy," Saudi J. Ophthalmol. **29**(2), 137–146 (2015).

21. J. Roider, N. A. Michaud, T. J. Flotte, and R. Birngruber, "Response of the retinal pigment epithelium to selective photocoagulation," Arch. Ophthalmol. **110**(12), 1786–1792 (1992).

22. J. Roider, F. Hillenkamp, T. Flotte, and R. Birngruber, "Microphotocoagulation: selective effects of repetitive short laser pulses," Proc. Nat. Acad. Sci. **90**(18), 8643–8647 (1993).

23. V. P. Gabel, R. Birngruber, and F. Hillenkamp, "Visible and near infrared light absorption in pigment epithelium and choroid," in *23rd Consilium Ophthalmologicum (Kyoto Excerpta Medica),* K. Shimizu, ed. (Elsevier, 1978), p.658–662.

24. G. Schuele, M. Rumohr, G. Huettmann, and R. Brinkmann, "RPE damage thresholds and mechanisms for laser exposure in the microsecond-to-millisecond time regimen," Invest. Ophthalmol. Vis. Sci. **46**(2), 714–719 (2005).

25. J. Roider, E. S. El Hifnawi, and R. Birngruber, "Bubble formation as primary interaction mechanism in retinal laser exposure with 200-ns laser pulses," Lasers Surg. Med. **22**(4), 240–248 (1998).

26. R. Brinkmann, G. Hüttmann, J. Rögener, J. Roider, R. Birngruber, and C. P. Lin, "Origin of retinal pigment epithelium cell damage by pulsed laser irradiance in the nanosecond to microsecond time regimen," Lasers Surg. Med. **27**(5), 451–464 (2000).

27. J. Neumann and R. Brinkmann, "Cell disintegration by laser-induced transient microbubbles and its simultaneous monitoring by interferometry," J. Biomed. Opt. **11**(4), 041112 (2006).

28. C. P. Lin, M. W. Kelly, S. A. Sibayan, M. A. Latina, and R. R. Anderson, "Selective cell killing by microparticle absorption of pulsed laser radiation," IEEE J. Sel. Top. Quantum Electron. **5**(4), 963–968 (1999).

29. J. Roider, S. H. M. Liew, C. Klatt, H. Elsner, E. Poerksen, J. Hillenkamp, R. Brinkmann, and R. Birngruber, "Selective retina therapy (SRT) for clinically significant diabetic macular edema," Graefe's Arch. Clin. Exp. Ophthalmol. **248**(9), 1263–1272 (2010).

30. M. Kim, Y. G. Park, S. H. Jeon, S. Y. Choi, and Y. J. Roh, "The efficacy of selective retina therapy for diabetic macular edema based on pretreatment central foveal thickness," Lasers Med. Sci. **35**(8), 1781–1790 (2020).

31. Y. G. Park, S. Kang, M. Kim, N. Yoo, and Y. J. Roh, "Selective retina therapy with automatic real-time feedback-controlled dosimetry for chronic central serous chorioretinopathy in Korean patients," Graefe's Arch. Clin. Exp. Ophthalmol. **255**(7), 1375–1383 (2017).

32. J. H. Yang, S. Y. Yu, T. G. Kim, E. S. Kim, and H. W. Kwak, "Morphologic changes in the retina after selective retina therapy," Graefe's Arch. Clin. Exp. Ophthalmol. **254**(6), 1099–1109 (2016).

33. R. Brinkmann, J. Roider, and R. Birngruber, "Selective retina therapy (SRT): a review on methods, techniques, preclinical and first clinical results," Bulletin De La Societe Belge D'Ophtalmologie **302**, 51–69 (2006).

34. C. Framme, G. Schuele, J. Roider, R. Birngruber, and R. Brinkmann, "Influence of pulse duration and pulse number in selective RPE laser treatment," Lasers Surg. Med. **34**(3), 206–215 (2004).

35. Y. M. Paulus, A. Jain, H. Nomoto, R. F. Gariano, and D. Palanker, "Selective retinal therapy with microsecond exposures using a continuous line scanning laser," Retina **31**(2), 380–388 (2011).

36. S. Muhammad, "Fundus fluorescein angiography," Journal of Postgraduate Medical Institute (Peshawar-Pakistan) 12(1) (1998).
37. G. Schuele, H. Elsner, C. Framme, J. Roider, R. Birngruber, and R. Brinkmann, "Optoacoustic real-time dosimetry for selective retina treatment," J. Biomed. Opt. 10(6), 064022 (2005).
38. S. Zbinden, Ş. S. Kucur, P. Steiner, S. Wolf, and R. Sznitman, "Automatic assessment of time-resolved OCT images for selective retina therapy," Int J CARS 11(6), 863–871 (2016).
39. T. Fountoukidou, P. Raisin, D. Kaufmann, J. Justiz, R. Sznitman, and S. Wolf, "Motion-invariant SRT treatment detection from direct M-scan OCT imaging," Int J CARS 13(5), 683–691 (2018).
40. D. Kaufmann, C. Burri, P. Arnold, V. M. Koch, C. Meier, B. Považay, and J. Justiz, "Selective retina therapy enhanced with optical coherence tomography for dosimetry control and monitoring: a proof of concept study," Biomed. Opt. Express 9(7), 3320–3334 (2018).
41. H. Lee, C. Alt, C. M. Pitsillides, and C. P. Lin, "Optical detection of intracellular cavitation during selective laser targeting of the retinal pigment epithelium: dependence of cell death mechanism on pulse duration," J. Biomed. Opt. 12(6), 064034 (2007).
42. E. Seifert, J. Tode, A. Pielen, D. Theisen-Kunde, C. Framme, J. Roider, Y. Miura, R. Birngruber, and R. Brinkmann, "Selective retina therapy: toward an optically controlled automatic dosing," J. Biomed. Opt. 23(11), 1 (2018).
43. P. Steiner, A. Ebneter, L. E. Berger, M. Zinkernagel, B. Považay, C. Meier, and R. Sznitman, "Time-Resolved Ultra–High Resolution Optical Coherence Tomography for Real-Time Monitoring of Selective Retina Therapy," Invest. Ophthalmol. Vis. Sci. 56(11), 6654–6662 (2015).
44. Y. G. Park, E. Seifert, Y. J. Roh, D. Theisen-Kunde, S. Kang, and R. Brinkmann, "Tissue response of selective retina therapy by means of a feedback-controlled energy ramping mode," Clin. Exp. Ophthalmol. 42(9), 846–855 (2014).
45. B. Považay, R. Brinkmann, M. Stoller, and R. Kessler, "Selective Retina Therapy," in *High Resolution Imaging in Microscopy and Ophthalmology*, (Springer, 2019), pp. 237–259.
46. A. Fritz, L. Ptaszynski, H. Stoehr, and R. Brinkmann, "Dynamics and detection of laser induced micro bubbles in the retinal pigment epithelium (RPE)," in *European Conference on Biomedical Optics*, (Optical Society of America, 2007), pp. 6632–6668.
47. F. C. Delori, R. H. Webb, and D. H. Sliney, "Maximum permissible exposures for ocular safety (ANSI 2000), with emphasis on ophthalmic devices," J. Opt. Soc. Am. A 24(5), 1250–1265 (2007).
48. M. A. Choma, C. Yang, and J. A. Izatt, "Instantaneous quadrature low-coherence interferometry with 3× 3 fiber-optic couplers," Opt. Lett. 28(22), 2162–2164 (2003).
49. S. Park, S. Rim, Y. Kim, and B. H. Lee, "Noncontact photoacoustic imaging based on optical quadrature detection with a multiport interferometer," Opt. Lett. 44(10), 2590–2593 (2019).
50. Y. Wang, Y. Hu, B. Peng, H. Zhou, Y. Zhao, and Z. Ma, "Complete-noncontact photoacoustic microscopy by detection of initial pressures using a 3×3 coupler-based fiber-optic interferometer," Biomed. Opt. Express 11(1), 505–516 (2020).
51. C. Xie, P. J. Winzer, G. Raybon, A. H. Gnauck, B. Zhu, T. Geisler, and B. Edvold, "Colorless coherent receiver using 3 (3 coupler hybrids and single-ended detection," Opt. Express 20(2), 1164–1171 (2012).
52. J. Neumann and R. Brinkmann, "Microbubble dynamics around laser heated microparticles," in *European Conference on Biomedical Optics* (Optical Society of America, 2003), pp. 5142–5182.
53. P. Deladurantaye, S. Méthot, O. Mermut, P. Galarneau, and P. J. Rochette, "Potential of sub-microsecond laser pulse shaping for controlling microcavitation in selective retinal therapies," Biomed. Opt. Express 11(1), 109–132 (2020).
54. E. I. Galanzha, E. V. Shashkov, P. M. Spring, J. Y. Suen, and V. P. Zharov, "In vivo, noninvasive, label-free detection and eradication of circulating metastatic melanoma cells using two-color photoacoustic flow cytometry with a diode laser," Cancer Res. 69(20), 7926–7934 (2009).
55. M. Sarimollaoglu, D. A. Nedosekin, Y. A. Menyaev, M. A. Juratli, and V. P. Zharov, "Nonlinear photoacoustic signal amplification from single targets in absorption background," Photoacoustics 2(1), 1–11 (2014).
56. W. J. Youden, "Index for rating diagnostic tests," Cancer 3(1), 32–35 (1950).
57. S. Lee, S. Wei, S. Guo, J. Kim, B. Kim, G. Kim, and J. U. Kang, "Selective retina therapy monitoring by speckle variance optical coherence tomography for dosimetry control," J. Biomed. Opt. 25(02), 1 (2020).
58. J. R. Stroud, L. Liu, S. Chin, T. D. Tran, and M. A. Foster, "Optical coherence tomography using physical domain data compression to achieve MHz A-scan rates," Opt. Express 27(25), 36329–36339 (2019).
59. D. J. Finney, *Probit Analysis*, 3rd ed., (Cambridge University Press, 1971).
60. C. Framme, G. Schuele, J. Roider, D. Kracht, R. Birngruber, and R. Brinkmann, "Threshold determinations for selective retinal pigment epithelium damage with repetitive pulsed microsecond laser systems in rabbits," Ophthalmic Surg Lasers Imaging 33(5), 400–409 (2002).
61. C. M. Moorman and A. M. P. Hamilton, "Clinical applications of the MicroPulse diode laser," Eye 13(2), 145–150 (1999).
62. J. M. Findlay, "Frequency analysis of human involuntary eye movement," Kybernetik 8(6), 207–214 (1971).
63. J. A. Gallego, E. Rocon, J. O. Roa, J. C. Moreno, and J. L. Pons, "Real-time estimation of pathological tremor parameters from gyroscope data," Sensors 10(3), 2129–2149 (2010).
64. K. V. Vienola, B. Braaf, C. K. Sheehy, Q. Yang, P. Tiruveedhula, D. W. Arathorn, J. F. de Boer, and A. Roorda, "Real-time eye motion compensation for OCT imaging with tracking SLO," Biomed. Opt. Express 3(11), 2950–2963 (2012).